Chinese Chemical Letters 37 (2026) 111650

Contents lists available at ScienceDirect

Chinese Chemical Letters

journal homepage: www.elsevier.com/locate/cclet

Sulfur vacancy-rich MoS_2 anchored oxidized graphene as advanced catalysts for polysulfide-iodine redox flow battery

Guolong Lu[a,1], Jingwen Zhang[a,1], Zhiwei Wang[a,1], Zhigui Wang[a,*], Yanhong Feng[a], Cejun Hu[b,*], Longchao Zhuo[c], Xijun Liu[a,*]

[a] MOE Key Laboratory of New Processing Technology for Nonferrous Metals and Materials, Guangxi Key Laboratory of Processing for Non-ferrous Metals and Featured Materials, School of Chemistry and Chemical Engineering, Guangxi University, Nanning 530004, China
[b] College of Materials Science and Engineering, Fuzhou University, Fuzhou 350108, China
[c] School of Materials Science and Engineering, Xi'an University of Technology, Xi'an 710048, China

ARTICLE INFO

Article history:
Received 11 June 2025
Revised 15 July 2025
Accepted 30 July 2025
Available online 30 July 2025

Keywords:
Sulfur vacancies
Graphene oxide
Aqueous redox flow battery
Bond bridging
High energy efficiency

ABSTRACT

Aqueous polysulfide/iodide redox flow batteries (SIRFBs) have been identified as a promising solution for scalable energy storage, exhibiting high energy density and cost-effectiveness, attracting considerable attention. Nonetheless, their practical applicability hindered by the suboptimal redox reaction kinetics, leading to constrained energy efficiency (EE) and power density. Herein, this study proposes a novel approach for coupling of graphene oxide with abundant sulfur vacancies in MoS_2 nanosheets (V_S-MoS_2@GO). The bifunctional catalysts enhancing the transformation of S^{2-}/S_x^{2-} and I^-/I_3^- redox couples while concomitantly improving the reaction kinetics. The experimental and theoretical calculation analyses elucidate that the GO bond with V_S-MoS_2 induces C-O-Mo and results in generating abundant sites, which attribute to the enhanced adsorption of crucial reaction intermediates and improved charge transfer. Consequently, the SIRFB derived notable EEs of 95.4%, 90.2%, and 75.6% at 10, 20, and 50 mA/cm^2 with 50% state of charge, respectively. Furthermore, these batteries exhibit remarkable power density (93.2 mW/cm^2), ultralow overpotential (100 mV), and an extended cycling life that exceeds 500 cycles. This work presents an innovative perspective to design high-active electrode materials that have potential for broad application in sundry flow battery chemistry, which would facilitate technological breakthroughs and advancements in the field of RFB.

© 2026 Published by Elsevier B.V. on behalf of Chinese Chemical Society and Institute of Materia Medica, Chinese Academy of Medical Sciences.

Renewable energy technology has undergone rapid development, thereby accelerating the progress of large-scale energy storage technology. This, in turn, has given rise to a need for a more flexible and cost-effective energy storage solution [1–3]. Aqueous redox flow batteries (RFBs) have garnered attention for their high scalability, design flexibility, capability to decouple power and energy, and enhanced safety [4–6]. The redox couple S^{2-}/S_x^{2-} and I^-/I_3^- could be designed as SIRFBs because of their low cost, excellent security, and high solubility [7]. However, the efficiency of SIRFBs is hindered by predominant charge transfer reactions within the polysulfides and the severe shuttle effect, resulting in elevated electrode polarization resistance and poor kinetic reversibility [8]. Consequently, it is necessary to design efficient electrode materials tailored for practical deployment in SIRFBs to enhance cost-effectiveness and power density and to stabilize energy efficiency (EE).

Recently, metal sulfides [9–15] have emerged as promising candidates due to their unique structural features and exceptional catalytic activity toward the S^{2-}/S_x^{2-} and I^-/I_3^-. Despite their proven advantages in boosting catalytic performance, their application in the SIRFBs remains limited. Two-dimensional transition metal dichalcogenides have garnered significant interest due to their excellent electrocatalytic properties and simple preparation methods [16,17]. Specifically, molybdenum disulfide (MoS_2) has garnered considerable attention due to its adjustable lateral size, exposure of active edge sites, and augmented specific surface area [18–20]. The edge structure of MoS_2 exhibits high catalytic activity, while the larger substrate area exhibits limited activity. In order to enhance the catalytic activity, it is necessary to activate the inert substrate, thereby acquiring additional active sites [21,22]. Graphene oxide (GO) possesses a considerable specific surface area and a high density of polar functional groups, garnering significant attention [23,24]. The incorporation of GO into MoS_2

* Corresponding authors.
E-mail addresses: 1608250348@qq.com (Z. Wang), cejun_hu@fzu.edu.cn (C. Hu), xjliu@gxu.edu.cn (X. Liu).
[1] These authors contributed equally to this work.

https://doi.org/10.1016/j.cclet.2025.111650
1001-8417/© 2026 Published by Elsevier B.V. on behalf of Chinese Chemical Society and Institute of Materia Medica, Chinese Academy of Medical Sciences.

has been shown to result in the creation of additional catalytic sites. This phenomenon is believed to be facilitated by van der Waals forces and a synergistic effect [25]. This approach aims to address the limitations of conventional SIRFBs, including limited kinetics, low conductivity, and suboptimal performance, presenting a valuable opportunity to contribute novel insights to the research field. Despite the notable advancements in this method for enhancing catalytic performance, its application in SIRFBs remains undocumented at this point.

In this work, a novel approach was employed to design a combination of GO with rich sulfur vacancies MoS_2 catalytic attached graphite felt electrodes (V_S-MoS_2@GO/GF) in the SIRFB system. The *in-situ* growth V_S-MoS_2@GO/GF exhibits a multitude of active sites, with the unsaturated edge Mo atom forming a bridge with the hydroxyl group on the surface of graphene oxide (C-O-Mo), thereby ensuring a smooth electronic pathway between the catalyst and the substrate. The experiments and theoretical calculations demonstrated that the formation of the C-O-Mo bond can expedite the electron transport rate. The combination of V_S has been shown to effectively enhance the catalytic activity, accelerating the redox reaction kinetics and thus improving the EE. The SIRFB employing V_S-MoS_2@GO/GF achieved a remarkable EEs of 95.4%, 90.2%, and 75.6% at 10, 20, and 50 mA/cm^2 with a 50% state of charge (SOC), respectively. Furthermore, the device exhibits an exceptional power density of 93.2 mW/cm^2, ultralow overpotential of 100 mV, and a remarkably extended cycle life of approximately 500 cycles during continuous operation at 10 mA/cm^2 with a 10% SOC.

The V_S-MoS_2@GO/GF hybrids were synthesized by a one-step solvothermal *in-situ* growth method. Prior to the initiation of the hydrothermal reaction, the GF underwent an acid activation process, which served to augment the number of active sites. In addition, the GO was loaded onto the GF through the process of freeze-drying and the utilization of H_2O_2 etching to stimulate S-vacancies (V_S) in the MoS_2. Subsequently, all raw materials were introduced into a Teflon tank containing the pretreated GF. Annealing, a process that occurs after the conclusion of the hydrothermal reaction with deionized (DI) water, serves to activate the material's structural integrity. The synthesis process for V_S-MoS_2@GO/GF is illustrated in Fig. 1a, and further detailed information can be found in the method section.

Scanning electron microscopy (SEM) images of GO/GF, V_S-MoS_2@GO/GF, and GF are depicted in Figs. 1b and c and Fig. S1 (Supporting information), respectively. These images reveal the GO as spun yarn adhere in the GF (Fig. 1b) and the V_S-MoS_2@GO/GF uniform distribution on the GF surface (Fig. 1c). V_S-MoS_2@GO/GF has been observed to form a flaky nanoflower structure, coating vertically aligned nanosheets (Fig. 1d). Further morphological analyses of V_S-MoS_2@GO using high-angle annular dark-field scanning transmission electron microscopy (HAADF-STEM) and energy-dispersive X-ray spectroscopy (EDX) mapping are presented in Figs. 1e and f. These images demonstrate a uniformly dispersed sheet material with C, O, S, and Mo elements, which is consistent with the morphology of V_S-MoS_2@GO. The transmission electron microscopy (TEM) image of V_S-MoS_2@GO is displayed in Fig. S2 (Supporting information), revealing folium and slice aggregate morphology, which resembles nebulous cloud flowers with a lateral size ranging from approximately 500–1000 nm.

Furthermore, high-resolution transmission electron microscopy (HRTEM) analysis of V_S-MoS_2@GO (Fig. 1g) revealed a layered lattice structure adhered to the GO. The presence of clear lattice fringes was measured, and the lattice spacing was found to be 0.661 nm and 0.663 nm, which is higher than that of MoS_2 (0.616 nm). This corresponds to the d values of the (002) plane (PDF #37-1492). The increase in the lattice of V_S-MoS_2@GO is attributed to the interaction between V_S-MoS_2 and GO, a hypothesis that will be validated through XRD and Raman analysis.

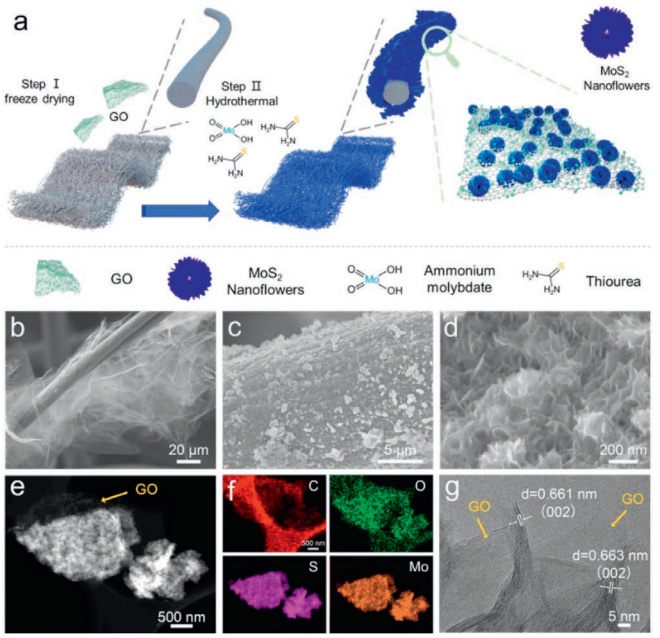


Fig. 1. (a) Scheme diagram for the V_S-MoS_2@GO/GF synthetic process. (b) SEM image of GO/GF. (c) SEM and (d) magnified images of V_S-MoS_2@GO/GF. (e) HAADF-STEM, (f) EDX, (g) HRTEM images of V_S-MoS_2@GO.

X-ray powder diffraction (XRD) measurements, Raman characterizations, and Fourier transform infrared spectroscopy (FTIR) were simultaneously conducted on MoS_2, V_S-MoS_2, and V_S-MoS_2@GO, and the results are shown in Figs. 2a-c. As illustrated in Fig. 2a, the XRD peaks of the three materials exhibit similar characteristic diffraction peaks at 14.4°, 33.5°, and 60.1°, which are consistent with the peaks of pristine MoS_2 (PDF #37-1492). This observation indicates that the XRD peaks of the three materials are analogous to the peaks of pristine MoS_2, suggesting that the materials are consistent in their crystal structure and diffraction patterns. The crystal structure of MoS_2 remains unchanged by the etching of H_2O_2 and the introduction of GO. As illustrated in Fig. 2a, the (002) planes of the characteristic peak (14.4°) in V_S-MoS_2@GO appear to be shifted to the left, indicating that the interlayer spacing of S-Mo-S has increased, while that of V_S-MoS_2 remains relatively unchanged [21,26]. This observation aligns with the results reported in the HRTEM study (Fig. 1g), suggesting a consistent pattern in the underlying mechanisms.

As illustrated in Fig. 2b (left graph), the Raman spectra of the samples reveal the characteristic peaks $E_{2g}{}^1$ (379 cm^{-1}) and A_{1g} (407 cm^{-1}) in MoS_2, V_S-MoS_2, and V_S-MoS_2@GO, corresponding to the vibration modes in-plane and out-of-plane of MoS_2 [27]. However, only the V_S-MoS_2@GO sample exhibits these two obvious peaks at 1351 and 1591 cm^{-1}, which is consistent with the characteristics of disordered carbon (D peak) and graphitic carbon (G peak) of GO. This observation indicates that V_S-MoS_2@GO was successfully constructed. As illustrated in Fig. 2b, the enlarged figure reveals the characteristic peaks $E_{2g}{}^1$ of V_S-MoS_2 and V_S-MoS_2@GO, which exhibit a left shift and broadening. This observation indicates that the Mo-S phonon pattern on the base plane has undergone a softening process. This softening can be attributed to a gradual decrease in Mo-S chemical bonds and an increase in V_S bonds within the plane [28,29]. In addition, the FTIR (Fig. 2c) demonstrates that the absorption peak (1050–1150 cm^{-1}) of C-O in V_S-MoS_2@GO is evidently greater than that of V_S-MoS_2 and MoS_2. This further suggests that a C-O-Mo bond is formed in the V_S-MoS_2 combined with GO [21].

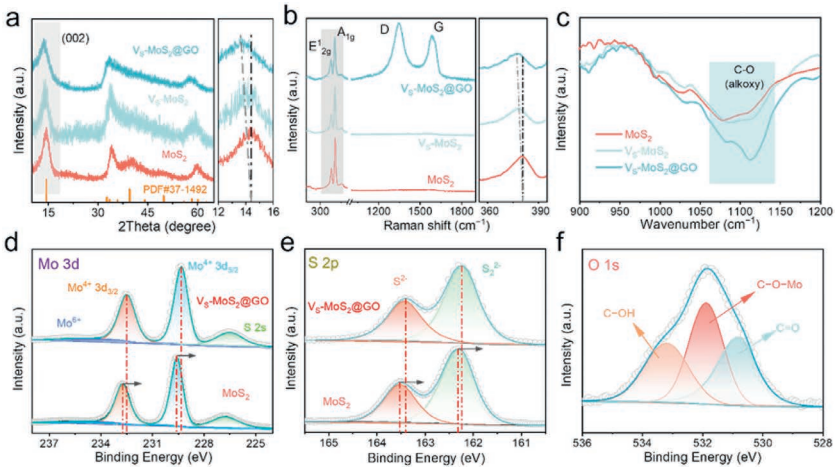


Fig. 2. (a) XRD patterns, (b) Raman spectra, and (c) FTIR spectra of MoS_2, V_S-MoS_2, and V_S-MoS_2@GO. (d) Mo 3d and (e) S 2p XPS spectra of MoS_2 and V_S-MoS_2@GO. (f) O 1s XPS spectrum of V_S-MoS_2@GO.

The X-ray photoelectron spectroscopy (XPS) images pertaining to MoS_2, V_S-MoS_2, and V_S-MoS_2@GO are presented in Figs. 2d-f and Fig. S3 (Supporting information). The purpose of this presentation is to further investigate the chemical compositions and bonding states of the MoS_2, V_S-MoS_2, and V_S-MoS_2@GO material. XPS provides direct evidence to explore the effect of V_S and GO condition. As illustrated in Fig. S3, a comparison is made between the XPS spectra of high-resolution Mo 3d and S 2p XPS spectra of MoS_2 and V_S-MoS_2. As illustrated in Fig. S3a, the spectrum exhibits two distinctive (red and blue) characteristic peaks at 229.9 and 232.8 eV, corresponding to Mo^{4+} $3d_{5/2}$ and Mo^{4+} $3d_{3/2}$, respectively [30]. Concurrently, two predominant (purple and green) peaks at 236.3 and 227.2 eV corresponding to Mo^{6+} and S 2s are observed [21,31]. Furthermore, the peaks of 163.5 and 162.2 eV could be assigned to S^{2-} and S_2^{2-} (Fig. S3b). A comparative analysis of the V_S-MoS_2 spectrum reveals a pronounced left shift in the main peaks of Mo 3d and S 2p. This shift can be attributed to the loss of electron cloud density around Mo and S, as well as a decrease in binding energy. The former is associated with the presence of an unsaturated Mo atom in MoS_2, while the latter is a consequence of the presence of a rich hydroxyl group bond on GO (C-O-Mo). As demonstrated in Fig. S4 (Supporting information), the EDX mapping of V_S-MoS_2@GO is consistent with the signals of Mo, S, C, and O. The atomic ratio of Mo and Co species in V_S-MoS_2@GO is documented in Table S1 (Supporting information). As illustrated in Figs. 2d and e, the high-resolution Mo 3d and S 2p XPS spectra of MoS_2 and V_S-MoS_2@GO, respectively, demonstrate a shift in the convolution peak of V_S-MoS_2@GO toward lower binding energy (right shift). This shift can be attributed to the increased electron cloud density resulting from the V_S in V_S-MoS_2, which exceeds the C-O-Mo bond shift. The superposition of these two effects, in addition to the shift of the peaks toward lower binding energy, is a key factor in understanding the observed phenomena [28]. Concurrently, the O 1s high-resolution spectrum (Fig. 2f) of the V_S-MoS_2@GO sample was deconvolved into three peaks (530.8, 531.9, and 533.2 eV), corresponding to the C=O, C-O-Mo, and C-OH bonds, respectively. This result indicates a C-O-Mo connection between V_S-MoS_2 and GO [32], which is consistent with the findings from XRD, Raman, and FTIR analyses. Besides, the sulfur vacancy of V_S-MoS_2@GO was verified by EPR spectrum (Fig. S5 in Supporting information), the symmetric signal in the range of 2.005 is observed, which is attributed to free electrons associated with S-vacancies. The higher peak intensity compared to bulk MoS_2 indicates the abundance of S-vacancies in V_S-MoS_2@GO [33].

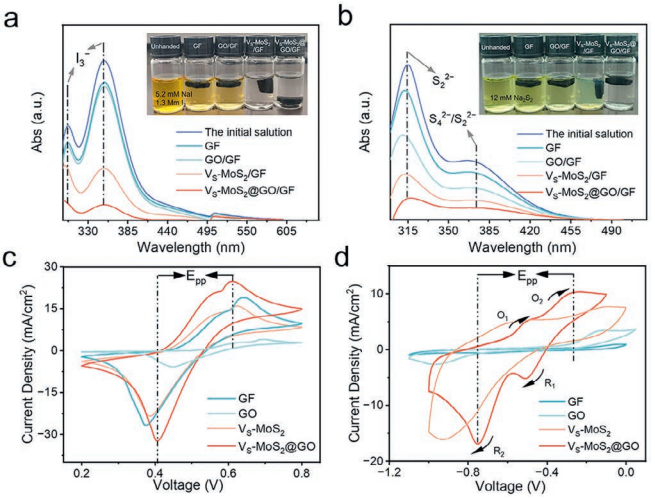


Fig. 3. UV-vis spectra of the (a) NaI + I_2 and (b) Na_2S_2 initial solutions as well as the solutions after interaction with GF, GO/GF, V_S-MoS_2/GF, and V_S-MoS_2@GO/GF. Inset: visualized adsorption of NaI + I_2 and Na_2S_2 with aqueous solutions on GF, GO/GF, V_S-MoS_2/GF, and V_S-MoS_2@GO/GF. CVs of the catalysts deposited on glassy carbon in (c) 0.1 mol/L NaI_3 + 0.5 mol/L NaCl solution and (d) 0.06 mol/L Na_2S + 0.02 mol/L S + 0.5 mol/L NaCl solution at a scan rate of 50 mV/s.

The adsorption behavior of redox species (S_x^{2-} and I_3^-) onto electrodes plays a vital role in the electrocatalytic process. As depicted in Fig. 3a, the NaI_3 aqueous solution in the presence of V_S-MoS_2@GO/GF and V_S-MoS_2/GF both exhibits more pronounced decolorization compared with solutions with GF and GO/GF, ultimately becoming a nearly colorless solution. However, in the ultraviolet-visible (UV-vis) absorption spectrum of the NaI_3 solution after adsorption with V_S-MoS_2@GO/GF revealed a further marked reduction in the typical absorption peaks associated with I_3^- ions compared to V_S-MoS_2/GF. These stark differences underscore the remarkable adsorption efficacy of V_S-MoS_2@GO/GF toward iodide species. The adsorption capacity of the materials for polysulfides was also explored (Fig. 3b), displaying a sequence analogous to their absorptivity toward iodide solutions. The adsorbing effect of V_S-MoS_2@GO/GF was clearly greater than that of V_S-MoS_2/GF for the intuitive adsorption phenomena.

The impact of V_S-MoS_2@GO on the electrocatalytic activity of S^{2-}/S_x^{2-} and I^-/I_3^- redox reactions was investigated and com-

pared using GF, GO, V_S-MoS_2, and V_S-MoS_2@GO electrodes by cyclic voltammetry (CV). As shown in Fig. 3c, each curve manifests a pair of peaks that correspond to the redox reactions of I^-/I_3^- couples when GF, GO, V_S-MoS_2, and V_S-MoS_2@GO electrodes are employed. The essential parameters for assessing the electrocatalytic properties of electrodes include peak-to-peak separation (E_{pp}) and peak current density [34], as outlined in Table S2 (Supporting information). It is noteworthy that V_S-MoS_2@GO demonstrates the most minimal E_{pp} (0.20 V) and the maximum peak current density, in contrast to V_S-MoS_2 (0.24), GO (0.25), and GF (0.27). This observation signifies that the GO bond with V_S is notably effective in facilitating the redox reaction of I^-/I_3^-. Furthermore, the $J_{Ox}/|J_{Red}|$ ratio of 0.761 for V_S-MoS_2@GO is higher than that of V_S-MoS_2 (0.678), GO (0.680), and GF (0.705), indicating higher reversible transformation and ingenious reactivity during the I^-/I_3^- redox reaction, favoring the reduction of the I_2 deposition. As illustrated in Fig. 3d, the V_S-MoS_2@GO electrode remarkably enhances the electrochemical reaction activity of the S_2^-/S_x^{2-} couple, resulting in multiple polysulfide redox peaks. In contrast, other electrodes manifest unintegrated and broad asymmetric peaks, such as two oxidation peaks and one reduction peak in the V_S-MoS_2, one oxidation peak and one reduction peak in the GO, while the oxidation peaks and reduction peaks exhibit weakness and almost no response in GF. The analysis of multiple electron transfers within the voltage range of −1.0 V ∼ 0.1 V *versus* Ag/AgCl reveals the presence of two oxidation peaks and two reduction peaks, suggesting the occurrence of more intricate electrochemical reactions involving various polysulfide species (*e.g.*, S_x^{2-}, where *x* ranges from 2 to 8). This behavior is consistent with observations in both aqueous and nonaqueous electrolytes [35,36]. The E_{pp} (Table S3 in Supporting information) of V_S-MoS_2@GO is 0.48, as seen in the S_2^-/S_x^{2-} reaction solution, which is smaller than that of V_S-MoS_2 (0.82), GO (0.84), and GF (0.91). Furthermore, the value of V_S-MoS_2@GO (0.604) indicates its superior reversibility to the S_2^-/S_x^{2-} redox reaction in comparison to that of V_S-MoS_2 (0.474). The value of the $J_{Ox}/|J_{Red}|$ ratio for the GO and GF is not a reference value because the peak and redox reaction are excessively small. Therefore, the results demonstrate that the V_S-MoS_2@GO sample exhibits superior catalytic activity and reaction kinetics for S^{2-}/S_x^{2-} and I^-/I_3^-. In addition, the linear sweep voltammetry (LSV) and Tafal slopes were shown in Fig. S6 (Supporting information), the V_S-MoS_2@GO exhibits the best reaction activity and smallest Tafel slope (130.4 and 60.1 mV/dec) than those of GF (284.7 and 154.7 mV/dec), GO (207.6 and 133.3 mV/dec), and V_s-MoS_2 (258.1 and 83.9 mV/dec) in S^{2-}/S_x^{2-} and I^-/I_3^- reaction system, showing the better reaction kinetics of the V_S-MoS_2@GO, according with the result of EIS.

Furthermore, the linear relationship between peak currents and the square root of the scan rate ($\nu^{1/2}$, Figs. S7 and S8 in Supporting information) manifests the S^{2-}/S_x^{2-} redox reaction of a diffusion-controlled process. The diffusion coefficient (D) of S^{2-}, as determined by the Berzins–Delahay equation, exhibits a sequence of values that corresponds to the order GF < GO < V_S-MoS_2 < V_S-MoS_2@GO. This observation aligns with the sequence of electrode catalytic capacity. The V_S-MoS_2@GO sample also have been implemented the CV activity test in the I^-/I_3^- redox reaction, which show that high-activity at the vary current density (Fig. S9 in Supporting information). Furthermore, the stability of V_S-MoS_2@GO, V_S-MoS_2 and MoS_2@GO for the S^{2-}/S_x^{2-} and I^-/I_3^- redox reactions is evident at 50 mV/s and 100 cycles (Fig. S10 in Supporting information). The V_S-MoS_2@GO shows remarkable stability and redox ability than that of V_S-MoS_2 and MoS_2@GO, which further prove that synergistic effect of V_S and C-O-Mo bond.

The enhancement in catalytic performance is attributed to the formation of a GO bond with V_S, resulting in the formation of a C-O-Mo bond. The total density of states (DOS) of GO, V_S-MoS_2, and V_S-MoS_2@GO was calculated (Fig. 4a). It is evident that the combination of V_S and GO induces spin polarization states, resulting in V_S-MoS_2@GO exhibiting the highest conductivity and affinity compared with V_S-MoS_2 and GO [29,37–39]. This phenomenon can augment the interfacial catalytic activity of V_S-MoS_2 for S^{2-}/S_x^{2-} and I^-/I_3^- because of its accelerated charge transfer speed. Further, V_S-MoS_2@GO has lower adsorption energy toward I^-, I_2, I_3^-, S^{2-}, S_2^{2-}, S_4^{2-}, S_6^{2-}, and S_8^{2-} intermediates as compared to those of V_S-MoS_2 and GO (Fig. S11 and Table S4 in Supporting information), demonstrating that V_S-MoS_2@GO present a higher affinity to those reaction intermediates. In addition, Fig. 4b presents the optimized geometry and differential charge density of V_S-MoS_2@GO. The yellow region and green region are indicative of the electron-rich region and electron-dispersion region, respectively. The electron cloud of V_S-MoS_2@GO undergoes a transformation, indicating that the C-O-Mo form facilitates electron transfer from V_S-MoS_2 to GO, thereby enhancing the electrical conductivity of V_S-MoS_2@GO. Furthermore, the generation of C-O-Mo, in conjunction with the presence of V_S, gives rise to electron rearrangement on the base plane of MoS_2. This electron-deficient state is more conducive to the adsorption of S^{2-}/S_x^{2-} and I^-/I_3^- on V_S-MoS_2@GO. The calculated results are consistent with the previously obtained XPS results.

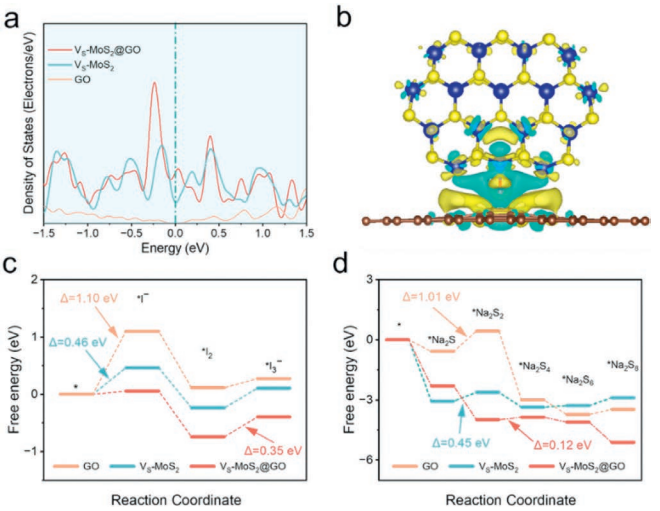


Fig. 4. (a) DOS of GO, V_S-MoS_2, and V_S-MoS_2@GO by DFT calculations. (b) The structural model of V_S-MoS_2@GO. Free-energy diagram of (c) I and (d) S intermediates for GO (orange), V_S-MoS_2 (blue), and V_S-MoS_2@GO (red).

In addition, density functional theory (DFT) calculations were conducted to elucidate the exceptional polysulfide/iodide species transformation activity exhibited by the V_S-MoS_2@GO. The binding free energies (ΔG) for the active species, namely $^*I^-$, $^*I_2$, and $^*I_3^-$, at the designated catalytic site were calculated (Fig. 4c). The ΔG values for $^*I^-$, $^*I_2$, and $^*I_3^-$ on GO were evident higher than those on V_S-MoS_2 and V_S-MoS_2@GO, implying the transformation of GO resistance is higher than that of other materials. Furthermore, the ΔG for $^*I^-$ was found to be lower on V_S-MoS_2@GO than on V_S-MoS_2 and GO, suggesting the high catalytic activity of V_S-MoS_2@GO, thereby facilitating the more facile adsorption and transformation of * to $^*I^-$. This outcome suggests that the transformation performance has been enhanced and made more accessible. It is noteworthy that V_S-MoS_2@GO requires relatively low transformation energy, and the transformation of $^*I_2$ to $^*I_3^-$ was identified as the rate-determining step. With V_S-MoS_2@GO (0.35 eV), a lower reaction energy barrier was exhibited than with GO (1.10 eV) and V_S-MoS_2 (0.46 eV), whose rate-determining step was identified as * to $^*I^-$. A similar trend was observed for the standard

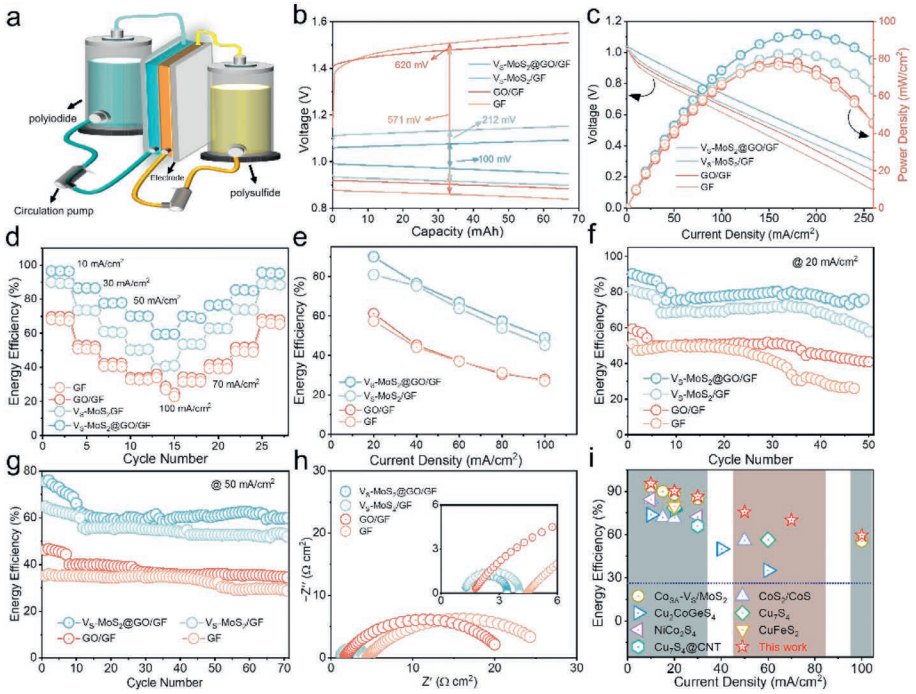


Fig. 5. (a) Scheme of the proposed SIRFB configuration. (b) The first charge and discharge curves of the SIRFB based on GF, GO/GF, V_S-MoS_2/GF, and V_S-MoS_2@GO/GF electrodes at 20 mA/cm^2 with 50% SOC. (c) Discharge polarization and power density curves of the SIRFB. (d) Rate performance with different current density. (e) Plots of EE at different operational current densities. Galvanostatic cycling EE of the SIRFB at (f) 20 mA/cm^2 and (g) 50 mA/cm^2 with 50% SOC. (h) EIS plots of the SIRFB with GF, GO/GF, V_S-MoS_2/GF, and V_S-MoS_2@GO/GF electrodes. (i) Comparison of properties with other sulfide electrode materials.

Gibbs free energy (ΔG) values associated with *, *Na_2S, *Na_2S_2, *Na_2S_4, *Na_2S_6, and *Na_2S_8 on GO, V_S-MoS_2, and V_S-MoS_2@GO (Fig. 4d). All sulfide species underwent spontaneous transformation, with V_S-MoS_2@GO facilitating a more accessible transformation process. Specifically, the transformation of polysulfide species, namely the conversion of *S^{2-} to *S_2^{2-} (on GO and V_S-MoS_2) and *S_2^{2-} to *S_4^{2-} (on V_S-MoS_2@GO), was promoted by V_S-MoS_2@GO with a lower Gibbs free energy (ΔG) of 0.12 eV compared with GO (1.01 eV) and V_S-MoS_2 (0.45 eV). As illustrated in Fig. S12 (Supporting information), a comprehensive array of molecular reaction simulations has been delineated. Consequently, the total density of states and the binding free energies of V_S-MoS_2@GO are greater than those of GO and V_S-MoS_2, suggesting that S^{2-}/S_x^{2-} and I^-/I_3^- interact more readily with V_S-MoS_2@GO, leading to enhanced conversion efficiency and reaction kinetics. This finding is in alignment with the prior visual outcomes observed in UV-vis and CV experiments. It has been demonstrated that the presence of the better ensures that the collision between the active substance and the electrode is more probable, thereby facilitating the gain and loss of electrons in the active substance and reducing the polarization of the SIRFB. A comprehensive review of the extant literature reveals a consistent pattern in the findings of experimental studies employing DFT simulations. These studies consistently demonstrate that the C-O-Mo bond coupling of V_S effectively facilitates the activity of I^-/I_3^- and S^{2-}/S_x^{2-} redox, thereby favoring the SIRFB performance.

Fig. 5a presents a schematic simulation representation of the proposed SIRFB construction. The assembly of SIRFBs was conducted by employing GF, GO/GF, V_S-MoS_2/GF, and V_S-MoS_2@GO/GF as anodic and cathodic electrodes (Fig. S13 in Supporting information). The anolyte utilized was 2.0 mol/L Na_2S_2, while the catholyte comprised 2.0 mol/L NaI and 0.5 mol/L I_2. A two-layer separator, consisting of G115 and K117, has been used to enhance the transportation of Na^+ cations and to restrict the cross-over of active species [40]. Fig. S14 (Supporting information) predominantly illustrates the initial deep charge and discharge curves of SIRFB based on the GF, GO/GF, V_S-MoS_2/GF, and V_S-MoS_2@GO/GF electrodes at 15 mA/cm^2 with deep charge and discharge (100% SOC). It is noteworthy that the V_S-MoS_2@GO/GF electrode exhibited the highest capacity at 111.6 mAh, surpassing the capacities of V_S-MoS_2/GF (85.1 mAh), GO/GF (82.8 mAh), and GF (70.2 mAh). Moreover, the polarization voltage difference for V_S-MoS_2@GO/GF is also evidently smaller than that observed for V_S-MoS_2/GF, GO/GF, and GF. Additionally, Fig. 5b illustrates a current density of 20 mA/cm^2 with 50% SOC, providing further insight into the remarkably small polarization voltage difference exhibited by V_S-MoS_2@GO/GF. It is evident that the initial charge and discharge polarization voltage difference of V_S-MoS_2@GO/GF (100 mV) is considerably lower than that of V_S-MoS_2/GF (212 mV), GO/GF (571 mV), and GF (620 mV). The low overpotential is indicative of the effective restraint of the side reaction, thereby reducing the generation of O_2/H_2. Concurrently, the reaction kinetics undergo a substantial acceleration [41]. Furthermore, the relationship curves of discharge polarization and power density for SIRFB are demonstrated in Fig. 5c, which indicates that the V_S-MoS_2@GO/GF electrode attains the maximum power density of 93.2 mW/cm^2, thereby surpassing GF (76.4 mW/cm^2), GO/GF (78.6 mW/cm^2), and V_S-MoS_2/GF (83.1 mW/cm^2).

The EEs of the SIRFB based on V_S-MoS_2@GO/GF, V_S-MoS_2/GF, GO/GF, and GF electrode with increasing current densities (10, 30, 50, 70, and 100 mA/cm^2) at the 50% SOC are shown in Fig. 5d. Conversely, an increase in the current density has been observed to result in an increase in the overpotentials and a concomitant decrease in the EEs of the SIRFB. The EEs of V_S-MoS_2@GO/GF show 96.5%, 86.4%, 77.8%, 69.9%, and 59.4%, respectively, which are all visibly higher than those of V_S-MoS_2/GF, GO/GF, and GF. This phenomenon can be attributed to the enhanced active surface area and reduced mass transport and ohmic resistances of the V_S-MoS_2@GO/GF in comparison with alternative electrodes [42]. A subsequent examination of the trends in coulombic efficiency (CE),

voltage efficiency (VE), and EE across successive various current densities (20, 40, 60, 80, and 100 mA/cm^2) for SIRFB is depicted in Fig. 5e and Figs. S15-S17 (Supporting information). The VE, representing the derivative of the CE and EE values (VE = EE/CE), consistently exhibits higher values than other at all current densities, thereby conforming to the variation trend of CE and EE (Figs. S15 and S16). The CE consistently maintains approximately 100% at employed current densities (Fig. S16). Concurrently, EE of V_S-MoS_2@GO/GF exhibits a decline, ranging from 90.1% at 20 mA/cm^2 to 49.0% at 100 mA/cm^2. This phenomenon is attributed to the augmented cell overpotential at elevated current densities (Fig. S17). As illustrated in Fig. 5f, the galvanostatic cycling performance of the SIRFB is demonstrated when operated at 20 mA/cm^2 with 50% SOC. The electrode composed of V_S-MoS_2@GO/GF exhibits the highest EE relative to other electrodes at the same charge/discharge current density, which is attributed to reduced charge/discharge overpotentials. Specifically, the SIRFB using V_S-MoS_2@GO/GF attains an initial EE of 90.2% at 20 mA/cm^2, accompanied by 84.0% capacity retention after 50 cycles. In addition, the VE and CE of the SIRFB, employing V_S-MoS_2@GO/GF electrodes with 50% SOC at 20 mA/cm^2, are replenished in Fig. S18 (Supporting information). The V_S-MoS_2@GO/GF electrode exhibited an initial VE of 90.2%, along with an exceptional CE of 100% in the first cycle. Notably, even after 50 cycles, VE and CE remained relatively high at 79.4% and 92.7%, respectively. The initial EE performance of V_S-MoS_2@GO/GF electrode exhibited superiority over that observed with bare GF and GO/GF electrodes, which yielded a lower EE of 50.7% and 59.3%, respectively. In contrast, the SIRFB employing V_S-MoS_2/GF as the electrode material exhibits an EE of 80.9% at 20 mA/cm^2, accompanied with a capacity retention of 57.8% after 50 cycles. This result further assesses the superior performance resulting from the synergistic effect of GO and abundant V_S. In addition, the durability of V_S-MoS_2@GO/GF was evaluated after the galvanostatic cycling test, the I-side electrodes were examined (Fig. S19 in Supporting information), and the results reveal that yellow substance is clearly observed on GF. By contrast, there is no I_2 residue exist on the surface of V_S-MoS_2@GO/GF, corroborating that V_S-MoS_2@GO/GF exhibits better activity towards I^-/I_3^- transformation and thus inhibits the I_2 production. As illustrated in Fig. S20 (Supporting information), the charge/discharge voltage profiles of the SIRFB, and the V_S-MoS_2@GO/GF electrode demonstrate a conspicuously diminished charge/discharge overpotential in comparison to that of alternative electrodes. Furthermore, the charge and discharge polarization curves further reveal that the open-circuit voltage condition of the V_S-MoS_2@GO/GF cell, which is consistent with the theoretical value of 1.02 V (Fig. S21 in Supporting information) [9,43].

Fig. 5g depicts the performance of SIRFB with regard to galvanostatic cycling EE of GF, GO/GF, V_S-MoS_2/GF, and V_S-MoS_2@GO/GF electrodes with 50% SOC at 50 mA/cm^2, and Fig. S22 (Supporting information) provides VE and CE regarding the V_S-MoS_2@GO/GF electrode. As the current density increases, the V_S-MoS_2@GO/GF electrodes exhibit a notable initial EE of 75.6%, with an EE of 60.0% after 70 cycles. Furthermore, the EE retention was found to be 75.8%, while the CE decreased from 100% to 96.7% over the course of 50 charge/discharge cycles. The collective presentation of results underscores the notable power densities and superior long-term cycling stability of the V_S-MoS_2@GO/GF electrode.

An investigation was conducted to ascertain the charge transfer resistance (R_{ct}), solution resistance (R_s), and electrode activity. This investigation utilized the technique of electrochemical impedance spectroscopy (EIS). The EIS plots for SIRFBs with different electrodes (Fig. 5h) with those simulated curves are shown in Fig. S23 (Supporting information), and the more detailed results are recorded in Table S5. The Nyquist plot revealed a semicircle corresponding to R_{ct} at the electrolyte–electrode interface. Specifically, the R_s values were determined to be 4.42, 1.61, 1.42, and 1.29 Ω/cm^2 for the GF, GO/GF, V_S-MoS_2/GF, and V_S-MoS_2@GO/GF electrodes, respectively. In accordance with these observations, the R_{ct} values were determined to be 22.97, 19.77, 2.70, and 2.11 Ω/cm^2 for the GF, GO/GF, V_S-MoS_2/GF, and V_S-MoS_2@GO/GF electrodes, respectively. These results underscore the ability of V_S-MoS_2@GO/GF to facilitate charge transfer and enhance diffusion dynamics, which is consistent with the findings of the CV experiments. Besides, the SIRFB catholyte, which employs GF, GO/GF, V_S-MoS_2/GF, and V_S-MoS_2@GO/GF electrodes, underwent extensive testing with multiple electrolyte refreshments to assess the long-term cycling stability of the electrodes (Fig. S24 in Supporting information). It is noteworthy that the V_S-MoS_2@GO/GF electrode demonstrated the highest initial EE of 95.4% when operated at 10 mA/cm^2. Furthermore, the EE demonstrated a capacity to regain a high value approaching the initial EE after refreshing the electrolyte in the 180th (94.7%) and 350th (94.1%) cycles, thereby substantiating the practical application value of the V_S-MoS_2@GO/GF electrode. Furthermore, EE was found to be stable at 62.1% after 500 cycles of continuous operation at 10% SOC. In contrast, the V_S-MoS_2/GF electrodes exhibited substantial degradation prior to attaining 180 cycles, while the GO/GF and GF electrodes demonstrated faster deterioration before reaching 100 cycles. Besides, the overall performance of GF, GO/GF, V_S-MoS_2/GF, and V_S-MoS_2@GO/GF electrodes are summarized in Table S6 (Supporting information). These findings demonstrate and underscore the robust stability and superior performance of the V_S-MoS_2@GO/GF electrode. The decline in the performance of the V_S-MoS_2@GO/GF electrode was attributed to the adsorption of S^{2-}/S_x^{2-} and I^-/I_3^- on the electrode surface, thereby hindering exposure of catalytically active sites.

In a comprehensive evaluation, the initial EE performance of V_S-MoS_2@GO/GF in different current densities (Fig. 5i), was compared with that of other recent sulfide electrode materials used in SIRFBs [9–11,13–15,43–46]. Besides, the integrated comparative analysis including maximum power density, initial voltage efficiency, and energy efficiency retention, indicating that the performance of V_S-MoS_2@GO/GF surpasses that of other sulfides, particularly in terms of maximum power density [47,48], where it demonstrates superiority (Fig. S25 and Table S7 in Supporting information). These findings substantiate the advantageous attributes of the electrode material with regard to the overall performance.

In this study, a self-supporting catalyst was successfully fabricated by combining GO into MoS_2 with abundant V_S. The catalyst, designated as V_S-MoS_2@GO/GF, was synthesized *via* a solvothermal method, resulting in the *in-situ* growth on a GF substrate. The bifunctional nature of V_S-MoS_2@GO/GF has been demonstrated to enhance the electrocatalytic activities of the S^{2-}/S_x^{2-} and I^-/I_3^- redox reactions. The GO bond with V_S facilitates the formation of abundant sites, thereby improving the adsorption of charged ions and promoting charge transfer. Experiment analysis and DFT calculations corroborate that the bond of C-O-Mo, in conjunction with V_S, augments the catalytic activity and adsorption capacity. The introduction of GO and V_S leads to a substantial reconstruction of the catalyst surface structure, resulting in activated GO and vacancy defects, and the formation of C-O-Mo bonds. This acceleration of the electron transport rate is accompanied by an improvement in catalytic activity, which in turn leads to enhanced rates of S^{2-}/S_x^{2-} and I^-/I_3^- redox reactions. These effects contribute to an augmentation in EE. Consequently, the SIRFB employing V_S-MoS_2@GO/GF achieved a remarkable EEs of 95.4%, 90.2%, and 75.6% at 10, 20, and 50 mA/cm^2 with a 50% SOC, respectively. Furthermore, the power density is measured at 93.2 mW/cm^2, ultralow overpotential of 100 mV, and the long cycle life is approximately 500 cycles during continuous operation at 10 mA/cm^2 with a 10% SOC. The

innovative design involving GO and abundant-vacancy nanoparticle electrocatalysts presents an effective strategy for enhancing the performance and competitiveness of related research.

CRediT authorship contribution statement

Guolong Lu: Writing – original draft. **Jingwen Zhang:** Data curation. **Zhiwei Wang:** Software. **Zhigui Wang:** Data curation. **Yanhong Feng:** Data curation. **Cejun Hu:** Supervision. **Longchao Zhuo:** Validation. **Xijun Liu:** Writing – review & editing, Supervision.

Declaration of competing interest

The authors declare that they have no known competing financial interests or personal relationships that could have appeared to influence the work reported in this paper.

Acknowledgments

This work was financially supported by the Guangxi Natural Science Fund for Distinguished Young Scholars (No. 2024GXNSFFA010008), and the National Natural Science Foundation of China (Nos. 22469002 and 22304028).

Supplementary materials

Supplementary material associated with this article can be found, in the online version, at doi:10.1016/j.cclet.2025.111650.

References

[1] J. Lei, Y. Zhang, Y. Yao, et al., Nat. Energy 8 (2023) 1355–1364.
[2] Z. Zhou, Y. Qian, X. Chen, et al., Adv. Funct. Mater. 34 (2024) 2404938.
[3] S. Fu, Y. Li, Y. Wang, China Powder Sci. Technol. 30 (2024) 27–40.
[4] D. Chao, W. Zhou, F. Xie, et al., Sci. Adv. 6 (2020) eaba4098.
[5] G. Lu, Z. Wang, S. Zhang, et al., Nanoscale 15 (2023) 4250–4260.
[6] X. Quan, W. Siyang, X. Chunming, et al., Chin. Chem. Lett. 34 (2023) 108188.
[7] Z. Li, G. Weng, Q. Zou, et al., Nano Energy 30 (2016) 283–292.
[8] L.F. Castañeda, F.C. Walsh, J.L. Nava, et al., Electrochim. Acta 258 (2017) 1115–1139.
[9] D. Ma, B. Hu, W. Wu, et al., Nat. Commun. 10 (2019) 3367.
[10] Y. Zhu, K. He, T.T. Tsega, et al., Sustain. Energy Fuels 4 (2020) 2892–2899.
[11] J. Zai, Y. Zhu, K. He, et al., Mater. Chem. Phys. 250 (2020) 123143.
[12] M. Gao, S. Huang, F. Zhang, et al., Mater. Today Energy 18 (2020) 100540.
[13] Y. Qin, X. Li, W. Liu, et al., Mater. Today Energy 21 (2021) 100746.
[14] J. Liu, L. Ren, Y. Wang, et al., J. Power Sources 561 (2023) 232607.
[15] T.T. Tsega, J. Zai, C.W. Lai, et al., Chin. J. Struct. Chem. 43 (2024) 100192.
[16] Y. Cao, ACS Nano 15 (2021) 11014–11039.
[17] Q. Fu, J. Han, X. Wang, et al., Adv. Mater. 33 (2021) 1907818.
[18] J. Kibsgaard, Z. Chen, B.N. Reinecke, et al., Nat. Mater. 11 (2012) 963–969.
[19] B. Sun, X. Li, J. Zheng, Mater. Rep. Energy 4 (2024) 100248.
[20] M. Yao, J. Yuan, B. Zhang, et al., Mater. Rep. Energy 4 (2024) 100251.
[21] J. Zhang, G. Xu, Q. Zhang, et al., Adv. Sci. 9 (2022) 2201579.
[22] Z. Zhao, Q. Dai, S. Huang, et al., Chin. Chem. Lett. 35 (2024) 109231.
[23] P. Kumari, A. Kumar, Y. Sabri, et al., Mater. Res. Bull. 180 (2024) 113037.
[24] D. Fengjun, Z. Tingyu, Z. Xiaochen, et al., Chin. Chem. Lett. 36 (2025) 109897.
[25] B. Chen, T. Wang, S. Zhao, et al., Adv. Mater. 33 (2021) 2007090.
[26] K.J. Huang, L. Wang, J.Z. Zhang, et al., Energy 67 (2014) 234–240.
[27] Q. Liu, Q. Fang, W. Chu, et al., Chem. Mater. 29 (2017) 4738–4744.
[28] X. Wang, Y. Zhang, H. Si, et al., J. Am. Chem. Soc. 142 (2020) 4298–4308.
[29] S. Najmaei, J. Yuan, J. Zhang, et al., Acc. Chem. Res. 48 (2015) 31–40.
[30] T. Wang, M. Li, L. Qi, et al., Adv. Funct. Mater. 33 (2023) 2308470.
[31] W. Ping, W. Ting, X. Ming, et al., Chin. Chem. Lett. 35 (2024) 108930.
[32] N.A. Kumar, M.A. Dar, R. Gul, et al., Mater. Today 18 (2015) 286–298.
[33] Y. Gao, Y. Deng, S. Xia, et al., Small 20 (2024) 2402412.
[34] Q. Zou, Z. Liang, G.Y. Du, et al., J. Am. Chem. Soc. 140 (2018) 10740–10748.
[35] Q. Zou, Y.C. Lu, J. Phys. Chem. Lett. 7 (2016) 1518–1525.
[36] M. Yang, X. Ren, L. Hu, et al., Chem. Eng. J. 412 (2021) 128628.
[37] M. Niu, W. Xin, L. Zhang, et al., Inorg. Chem. Front. 11 (2024) 2272–2280.
[38] X. Liu, M. Chen, J. Ma, et al., China Powder Sci. Technol. 30 (2024) 35–45.
[39] J. Yang, F. Zhang, J. Chen, China Powder Sci. Technol. 30 (2024) 161–170.
[40] Z. Li, Y.C. Lu, Nat. Energy 6 (2021) 517–528.
[41] J. Wang, L. Yu, L. Hu, et al., Nat. Commun. 9 (2018) 1795.
[42] M. Rahimi, A. Molaei Dehkordi, H. Gharibi, et al., Ind. Eng. Chem. Res. 60 (2021) 824–841.
[43] Z. Wang, G. Lu, T. Wei, et al., Nat. Commun. 16 (2025) 2885.
[44] J. Li, R. Li, J. Liu, et al., Chin. Chem. Lett. 35 (2024) 110355.
[45] S. Qiu, Y. Zhao, K. Wang, J, et al., Mater. Rep. Energy 4 (2024) 100293.
[46] X. Zhao, X. Niu, X. Liu, et al., Mater. Rep. Energy 4 (2024) 100271.
[47] L. Yang, X. Huang, H. Shan, et al., China Powder Sci. Technol. 30 (2024) 113–121.
[48] K. Duan, Y. Feng, Q. Liu, et al., ChemSusChem 18 (2025) 2500833.